Ultra-efficient in-core acoustic waves in suspended core fiber for high frequency fiber-optic ultrasonic devices

Ricardo E. da Silva* **and David J. Webb**

Aston Institute of Photonic Technologies, Aston University, Birmingham, B4 7ET, U.K.

*Email: r.da-silva@aston.ac.uk

High frequency acoustic waves confined inside a suspended core fiber (SCF) are revealed by numerical simulations for the first time. A standard optical fiber (SMF) is modelled to explain the current research limitations. The acoustic frequency response and energy concentrated in both fibers are evaluated from 50 to 56 MHz with the 3D finite element method. The simulated dispersion curves are compared to the Pochhammer-Chree solutions. The energy in the SCF core at the resonance of 52.84 MHz is approximately 16 times higher compared to the SMF, indicating a new route for the design and fabrication of fiber-based ultrasonic devices.

Ultrasonic waves have been successfully employed to modulate optical fibers in notch filters, frequency shifters, dynamic couplers, Q-switched and mode-locked fiber lasers[1–6]. Acousto-optic modulators are tuned by the acoustic power and frequency, providing low insertion losses and easy integration with fiber optic components. In particular, the interaction of standing longitudinal acoustic waves and fiber Bragg gratings (FBGs) is suitable to mode-lock the repetition rate of fiber lasers at twice the acoustic frequency. The acoustically induced displacements compress and extend the grating period, inducing reflection bands on both sides of the Bragg wavelength [7]. Constant acoustic amplitude and period are therefore important requirements to accurately tune the grating reflectivity with stable output operation.

However, in standard fibers, the acoustic energy is distributed throughout the cladding, reducing the interaction with the optical modes in the core. Long interaction lengths, high acoustic powers, cladding-etched and tapered fibers have been employed to increase the acousto-optic interaction [6,8]. Nevertheless, the reduction of the fiber diameter degrades the optical/mechanical stability, while long lengths increase the switching time. The decreasing acoustic energy in the core becomes critical with the variation of the acoustic velocity and the emergence of higher order modes with increasing frequency, limiting the operation of current devices to frequencies up to approximately 10 MHz [9].

Figs. 1(a)-1(c) illustrate the displacements **u** in a standard single mode optical fiber (SMF) with increasing frequency *f*. Longitudinal acoustic waves are axially symmetric waves characterized by radial *v* and axial *w* displacement components given by [9,10],

$$v = \{-pAJ_1(pr) - ikCJ_1(qr)\}exp\left[i(kz-\omega t)\right], \quad (1)$$

$$w = \{ikAJ_0(pr) + qCJ_0(qr)\}exp\left[i(kz-\omega t)\right], \quad (2)$$

in which, $p^2 = (\omega^2 / c_D^2) - k^2$, $q^2 = (\omega^2 / c_T^2) - k^2$, are expressed in terms of the dilatational c_D and transversal c_T material velocities,

$$c_D^2 = \frac{\gamma + 2\mu}{\rho}, \qquad c_T^2 = \frac{\mu}{\rho}, \quad (3)$$

Lamé elastic constants, γ and μ, and density ρ. J_0 and J_1 are Bessel functions of the first kind, $k=2\pi/\lambda_b$, is the wavenumber, $\omega=2\pi f=kc_P$, is the angular frequency, and A and C are arbitrary constants. The axial and radial displacements exchange over the fiber cross section with the radius r. The fiber diameter is $2a$.

As $ka\rightarrow 0$, the phase velocity c_P approaches the extensional velocity $c_E=(Y/\rho)^{1/2}$, where Y is the Young's modulus. Consequently, the axial displacements are predominantly distributed over the fiber cross section (Fig. 1(a)). As $ka\rightarrow\infty$, c_P approaches the velocity of Rayleigh surface waves [11],

$$c_R \sim \left(\frac{0.87+1.12\upsilon}{1+\upsilon}\right)c_T, \quad (4)$$

in which, υ is the Poisson's ratio. The kinetic energy density, $\mathbf{E} = \frac{1}{2}\rho\omega^2(|u|^2 + |v|^2 + |w|^2)$, propagates in the fiber with the group velocity, $c_g = \partial\omega/\partial k$, as [9],

$$c_g = \frac{c_P}{1-(\omega/c_P)(\partial c_P/\partial\omega)}. \quad (5)$$

Most of the displacements are radially distributed at low values of c_g (Fig. 1(b)). Fig. 1(d) shows the modulus variation of w and v for the fundamental acoustic mode (l_{01}), indicating null (dark blue color) and maximum (dark red color) displacements.

The axial displacements are partially replaced by the radial components over the fiber cross section with increasing frequency f [9]. Fig. 1(c) illustrates the displacements around 50 MHz. The wavenumbers k of the free-vibration modes are computed with the finite element

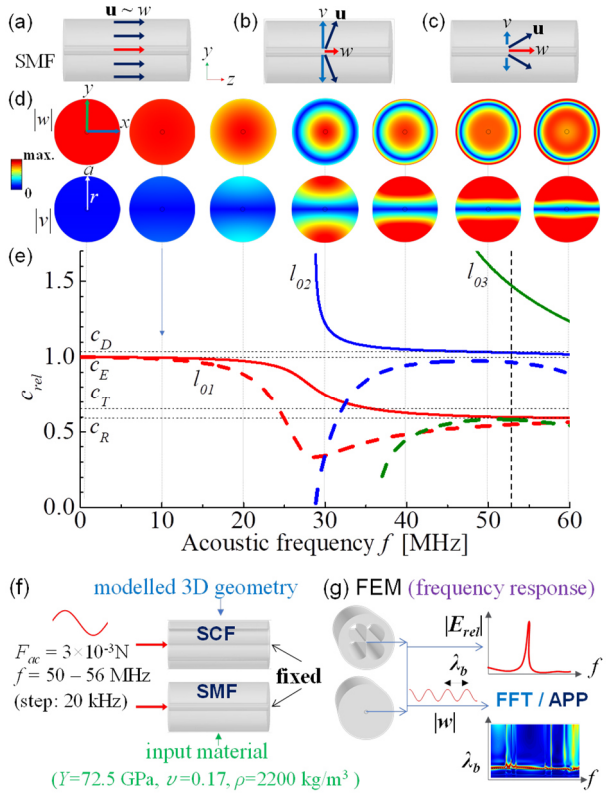

Fig. 1. Illustration of the axial w and radial v displacements exchanging with the frequency in a SMF: (a) up to 10 MHz, and approximately (b) 30 MHz and (c) 50 MHz. (d) Distribution of w and v for the fundamental mode l_{01}. (e)Phase velocity (solid lines) and group velocity (dashed lines) for l_{01} and higher order modes l_{02} and l_{03}. (f) Modelling, input parameters and boundary conditions applied to the SCF and SMF. (g) The energy confinement $\mathbf{E}_{rel}$ and displacements w are computed by the FEM. The dispersion curves are calculated by the FFT and APP methods.

method (FEM) [12–16]. Fig. 1(e) shows the simulated phase velocities c_P (solid lines) compared to c_D, c_T, c_R and c_g, calculated with Eqs. (3), (4) and (5) (the velocities are normalized to c_E). The fiber cross section becomes multimode at frequencies approaching 30 MHz in which the acoustic period λ_b is comparable to the fiber diameter.

In this paper, we have investigated the modal superposition and energy confinement in the cores of a standard optical fiber and a suspended core fiber (SCF) [4,13,17] at frequencies higher than 50 MHz. In this range, the SMF cross section supports two higher order modes with distinct displacement patterns, phase and group velocities (modes l_{02} and l_{03} in Fig. 1(e)). The overlapping between the modes transfers energy from the fiber core to the cladding and surface, inducing distortion of the wave amplitude and period. As a promising alternative, we propose monomode operation in the fiber core by modal acoustic filtering with SCFs.

We have modelled a SMF-28 and a SCF of 500 µm length and 125 µm diameter. The SCF model is based on a real fiber [4], with a 5 µm diameter (D) core suspended by four air holes with a diameter of ~45µm. The silica bridges are ~700 nm in thickness. The bridge length (d) is ~27 µm. Both fibers are composed of silica: Young's modulus Y=72.5 GPa, Poisson ratio ν=0.17 and density ρ=2200 kg/m^3 [9,13]. A sinusoidal acoustic force with amplitude F_{ac}=3×10^{-3}N is axially applied at one end of the fibers from f = 50 to 56 MHz (20 kHz steps), as illustrated in Fig. 1(f). The other fiber end is fixed. The frequency response is calculated by means of the finite element method (FEM) included in the commercial package COMSOL Multiphysics 5.4, employing the methodology described in Refs.[2,12,13,15,16]. The simulations are computed with a High-Performance Computer cluster (HPC) equipped with 2000 processor-cores and 9TB memory.

The axial displacements w are computed in the core center (r=0) of both fibers. The wavelength λ_b of the modal superposition is estimated from $|w|$ by employing the fast Fourier transform (FFT)[18,19], as illustrated in Fig. 1(g). The FFT peaks are fitted with a cubic spline interpolation function and normalized to emphasize the predominant wavelength λ_b (dark red color in Figs. 2(a) and 2(b)). λ_b is also computed by averaging the distance between consecutive wave peaks and nodes along the fiber (averaged peak-to-peak (APP)). This method provides high accuracy to measure periodic waves. Overlapping between the FFT/APP curves indicates waves approaching constant amplitude and period. The kinetic energy density $\mathbf{E}$ is integrated along the SCF core and bridges and along the SMF core. The efficiency of the energy confinement $\mathbf{E}_{rel}$ is evaluated by comparing the energy in the core with the total energy stored in the fiber.

The wavelength λ_b of the three acoustic modes supported by the SMF for the considered frequency range is calculated by means of the well-known Pochhammer-Chree theory [20,21]. The wavenumber in Eqs. (1) and (2) are numerically computed by employing the same parameters of the simulations, and the method and algorithms proposed in Refs.[22–25]. The same procedure is employed to compute the wavelength λ_b of the mode confined inside the SCF core, considering the fiber core as a perfect cylindrical waveguide.

Figures 2(a) and 2(b) show the 2D FFT spectrum compared to APP (white line) and the theoretically calculated modes (black lines) for the SMF and SCF. The displacements of the acoustic modes are shown in steps of f = 1 MHz in Fig. 2(c). The resonance peaks in Fig. 2(d) show the comparison between the energy confined in the SCF and SMF, $\mathbf{E}_{rel}$. Fig. 2(a) shows variations of λ_b caused by the superposition between the three modes. The difference between FFT and APP methods indicates distortion of the sinusoidal wave pattern caused by modes overlapping out-of-phase or transversally to the fiber length (e.g. as indicated by the regions delimited by white dashed lines). As defined in Eqs. (1) and (2), the axially symmetric modes are characterized only by radial v and axial w displacement components (Figs. 1(a)-1(c) illustrate these components with vectors for the fundamental mode in a SMF. The superposition of the

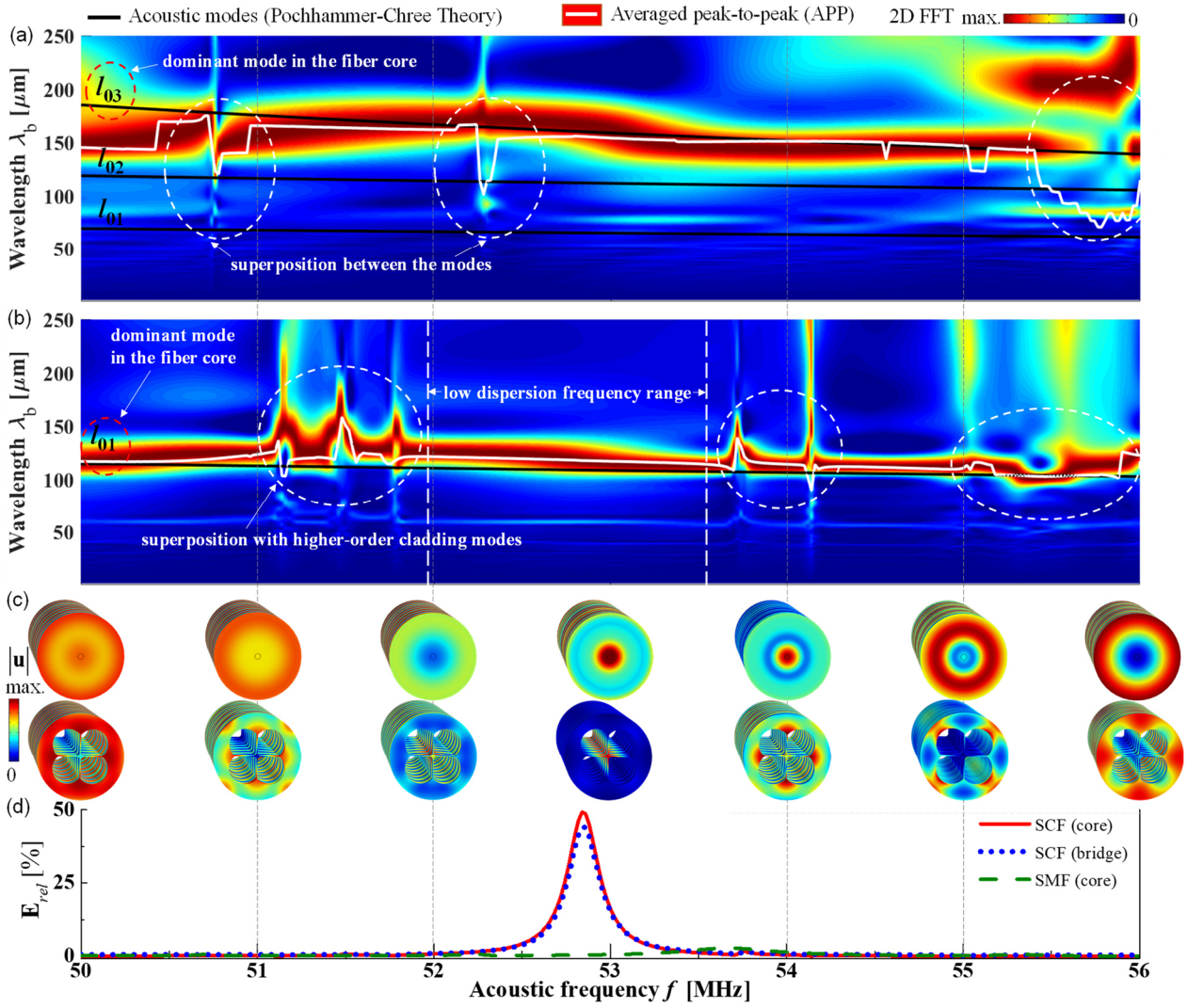

Fig. 2. Wavelength λ_b variation for the (a)SMF and (b)SCF computed with the 2D FFT and APP methods for f=50-56 MHz The simulations are compared to the Pochhammer-Chree theoretical modes (black lines). (c) Displacement patterns are shown in 1 MHz steps. (d) The efficiency of energy confinement $\mathbf{E}_{rel}$ in the SCF and SMF.

modes is therefore the basic algebraic sum of the components (vectors) of the considered individual modes. The high agreement between the simulated FFT and theoretical curves of 98% (averaged over the frequency range) indicates the higher-order mode l_{03} as the dominant mode in the fiber core. The energy is mostly distributed in the cladding and surface, reducing the overall energy in the SMF core to a maximum of 3% in Fig. 2(d).

Oppositely, the energy is concentrated in the bridges (44%) and core (49%) for the SCF resonance in Fig. 2(b), inducing strong confinement inside the fiber (93%) at f_c=52.84 MHz. The clear region around the resonance in the FFT spectrum and the agreement between the APP and theoretical curves of 94% indicates just one mode (l_{01}) with an almost sinusoidal pattern in the SCF core. Higher agreement with theoretical values are expected by employing SCFs approaching a circular shaped core and reducing the superposition with higher order cladding modes (white dashed lines in Fig. 2(b)). Overall, distortion of the wave amplitude and period is reduced for the whole frequency range compared to the SMF.

We have evaluated the superposition between the acoustic modes inside the SMF and SCF at f_c=52.84 MHz (frequency indicated as a vertical dashed line in Fig. 1(e)). Fig. 3(a) shows the 3D displacements in the SMF being evaluated along the yz plane (Fig. 3(b)). $|\mathbf{u}|$ is decomposed into the radial v and axial w components in Figs. 3(c) and 3(d). Fig. 3(g) shows v and w normalized to the maximum at the radial positions indicated in Fig. 3(a). The overlapped radial pattern of the fundamental mode l_{01} is shown as a detail in Fig. 3(c). The axial pattern of l_{01} is not visible because it overlaps the higher order modes l_{02} and l_{03} (Figs. 3(e) and 3(f)). Note that strong radial couplings induce 90° shifted axial displacements along the fiber (e.g. vertical green line). Fig. 3(g) shows distortion of the wave

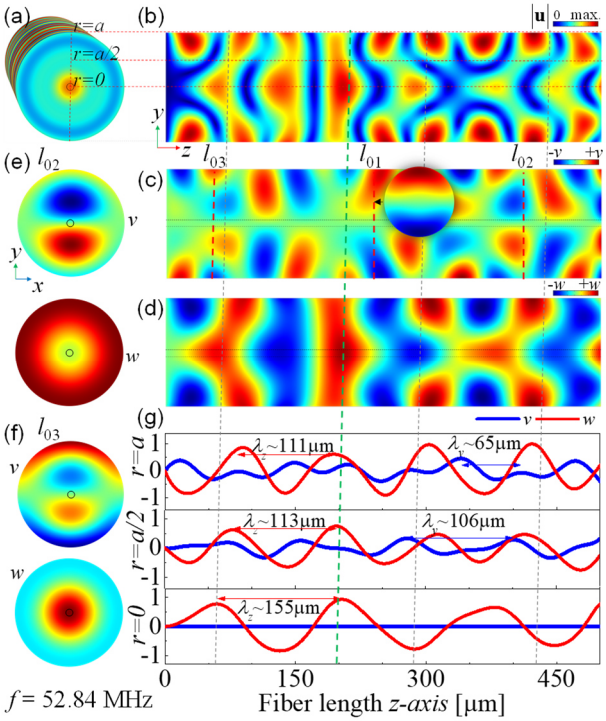

Fig. 3. (a) 3D SMF displacements evaluated in the (b) *yz* plane. (c) radial *v* and (d) axial *w* components show the overlapping between the fundamental l_{01} and higher order modes (e) l_{02} and (f) l_{03}. (g) Wavelength λ_b is evaluated as indicated in Fig. 3(a).

amplitude and period in the core center caused by the modes overlapping nonuniformly and out-of-phase over the fiber cross section. The physical mechanism underlying the results in Fig. 3 are defined by the dispersion of the acoustic waveguide in the considered frequency range. In other words, the fiber cross section works as a transversal acoustic cavity which is resonant with the modal field of higher order modes after a specific frequency. The sinusoidal wave pattern with constant amplitude and wavelength of the fundamental mode illustrated in Fig. 1(a) (up to 10 MHz) is replaced by a complex wave pattern, as seen in Fig. 3(g). The dispersion causes the fundamental mode to concentrate mostly over the fiber surface, as indicated in the cross section of l_{01} in Fig. 3(c) and the shortest wavelength in Fig. 3(g). The increasing wavelength in Fig. 3(g) shows the influence of the higher order modes in the fiber, indicating the dominance of l_{03} in the core center ($r = 0$), as indicated with the axial displacement *w* in Fig. 3(f).

Figs. 4(a) and 4(b) show the displacement distribution in the SCF, decomposed into the transversal *v* and axial *w* components (Figs. 4(c) and 4(d)). Fig. 4(g) shows *v* and *w* at the radial positions in Fig. 4(a). The displacement pattern over the silica bridges has distinct transversal (A_1) and axial (S_0) components[10]. A_1 is antisymmetric in relation to the fiber axis and S_0 is symmetric in relation to the line perpendicular to the fiber axis [26]. The *xy* patterns of A_1 and S_0 are shown in Fig. 4(e) and 4(f). S_0 achieves a maximum at the core center (r=0) inducing a longitudinal acoustic wave with constant period λ_b and amplitude (Fig. 4(g)). In contrast, the displacements on the fiber surface (r=a) have a maximum amplitude of ~3% compared to the core. Considering that these low displacements have no significant effect on S_0[26], the resonant wavenumber k_b=$2\pi/\lambda_b$ is estimated as[14,26],

$$k_b L_b \sim \pi\left(1-\frac{1}{8}\pi^4\left(\frac{D}{L_b}\right)^4\right), \qquad (6)$$

in which, L_b is the effective total bridge length, and D is the core diameter ($D/L_b \leq 0.1$). Solution of Eq. (6) shows that the silica bridges and core are resonant with half wavelength λ_b (L_b~$\lambda_b/2$), as seen in Figs. 4(d) and 4(f). Therefore, tuning of f_c is expected by changing the bridge length, or with minor effect, the core diameter. Frequency shifts of f_c caused by changes of the fiber length are also expected. The results show that the SCF is considerably less affected by dispersion compared to the SMF. Although the evidence of higher order modes is still observed over the fiber surface and cladding (yellow shadows in Fig. 4(e) and 4(f)), the influence of these modes in the fiber core is irrelevant. The reduced dispersion is confirmed by a smaller wavelength in the core center ($r = 0$) compared to the SMF, as seen in Fig. 4(g). The sinusoidal pattern in the fiber core shows the existence of just one mode in the core, which is suitable for acousto-optic modulation, as has been demonstrated for frequencies lower than 10 MHz. In fact, the waveguide diameter is significantly reduced to 5 μm (fiber core) imposing a strong filtering to higher other modes with transversal fields considerably larger than this value. For practical applications, the dispersion phenomenon is adjusted by evaluating the ratio of between the waveguide diameter and the period of the acoustic waves at a specific acoustic frequency.

The theory described by Eqs. (1) to (5) provides a basic understanding about the definition of longitudinal acoustic waves and the main parameters used as reference in acoustic waveguides. Our numerical investigation aims to provide a practical, versatile and detailed alternative in comparation to the complex and extensive Pochhammer-Chree equations, describing the propagation of longitudinal modes in an infinite, isotropic, homogeneous and solid cylindrical waveguide. The solution of those equations has been computed by employing a combination of numerical methods included in the algorithms proposed by Puckett in Ref. 25. The modes' wavenumbers (wavelength, phase and group velocities) are calculated for each acoustic frequency, considering the fiber´s geometry and material as input parameters. The dispersion curves (wavelength vs frequency) are calculated individually for each mode, as seen in Figs. 2(a) and 2(b). In contrast, the 3D simulation provides a tool for the design and evaluation of the overall device, including additional parameters necessary for the manufacture and efficient operation. It enables the study of the real situation in which the resonant

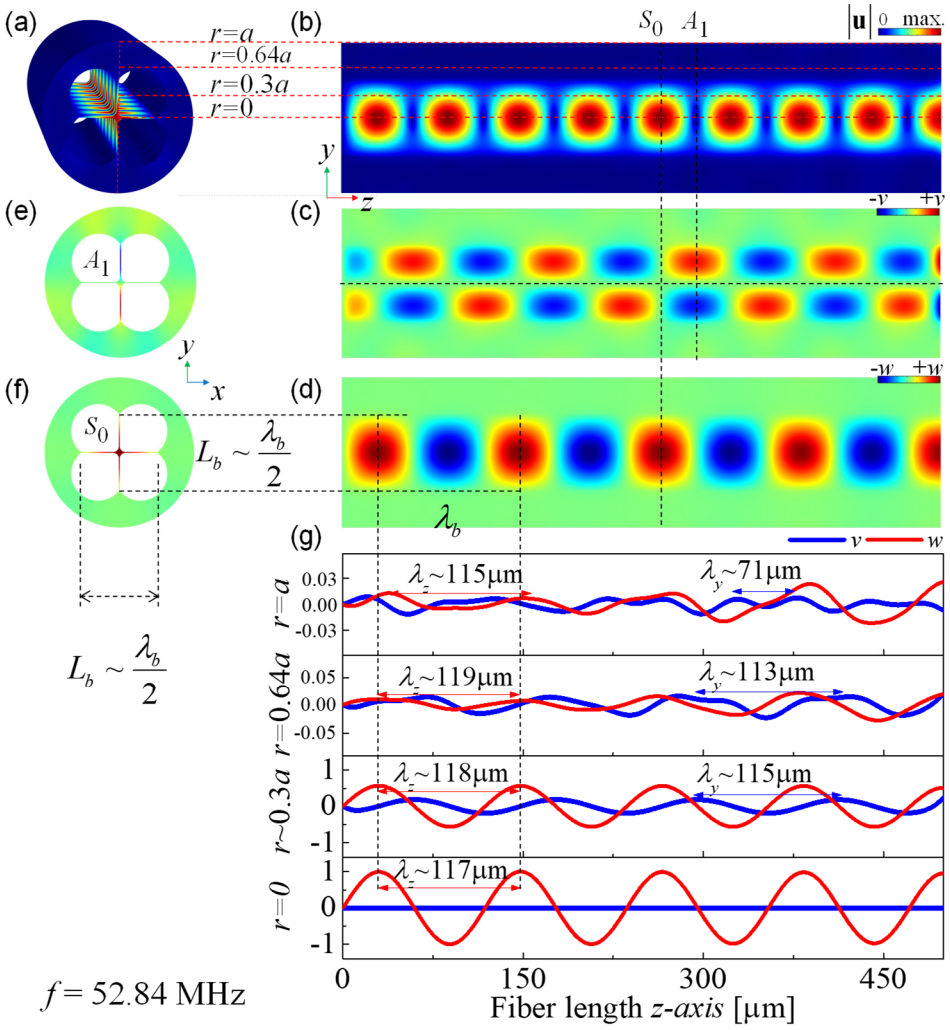

Fig. 4. (a) 3D SCF displacements evaluated in the (b) *yz* plane. (c) Transversal *v* and (d) axial *w* components show the (e) antisymmetric A_1 and (f) symmetric S_0 wave patterns. (g) Wavelength λ_b is evaluated as indicated in Fig. 4(a).

modes are excited simultaneously in the fibers, in which one dominates over the others in a specific frequency range.

The acoustic waves excited in the core of the optical fibers at higher frequencies show a complex non-sinusoidal envelope caused by the superposition of the modes. The direct evaluation of the wave amplitude in the space domain (acoustic amplitude along the fiber length) for each frequency is elaborate and may be impracticable to evaluate a large number of samples (300 samples are analyzed for the considered frequency range). The FFT evaluates efficiently all these samples and calculates the acoustic wavelength of the mode or modes contributing to the complex acoustic amplitude. The analyses of the wavelengths in the frequency domain identifies the modes and how the acoustic waves deviate from a sinusoidal pattern with constant amplitude and period (ideal case for practical applications). The FFT therefore indicates the most suitable frequency range for the efficient operation of the acousto-optic devices. Considering that the devices are driven by an electrical signal, the dispersion curves show the frequencies in which the devices are properly tuned to have a higher modulation efficiency (e.g. the frequency range from 52 to 53.5 MHz in Fig. 2(b)).

Further advance of this study might suggest the evaluation of the relative amplitude of each mode in the modal superposition. It might be achieved by considering the third axis of the FFT at a specific frequency (e. g. evaluation of the acoustic amplitude versus the wavelength). The experimental assembly of the proposed device might require the modelling of the real SCFs geometry and material considering defects, imperfections, or dimension changes, which could shift the resonance and reduce the effective overall energy in the core. Microcavities based on SCFs might be achieved with good optical and mechanical properties by employing advanced splicing and alignment techniques[27].

Overall, the achievements and methodology proposed in this research are promising for the design and fabrication of acousto-optic modulators and fiber-based ultrasonic sensors, especially those composed of fiber Bragg gratings[28–30]. The combination with FBGs enables a

distinct advantage to measure simultaneously the acoustic field and temperature [31]. The high acoustic sensitivity in the SCF core is significantly promising to improve the noise-limited pressure resolution and frequency operation of optoacoustic devices, contributing to compact and efficient all-fiber devices for biomedical applications [30].

In summary, we have numerically investigated the modal superposition and energy confinement in the cores of a SMF and a SCF from 50 to 56 MHz. For the SMF, coupling between modes reduces the acoustic energy in the core. Distortion of the wave amplitude and period is observed. Energy distribution on the fiber surface with increasing frequency is expected, since the modes tend to propagate as Rayleigh waves. We have proposed a potential solution to increase the frequency operation of the current all-fiber ultrasonic devices by efficiently confining the acoustic energy inside SCFs. The wave periods must be comparable with the total bridge length. Multimode overlapping in the fiber core is considerably reduced for the 6 MHz frequency range, approaching a monomode dispersionless bandwidth around the resonance at f_c=52.84 MHz. High energy in the SCF core will certainly strengthen the interaction with the optical modes and Bragg gratings, making possible acoustic modulation of fiber lasers with repetition rates higher than 100 MHz.

Acknowledgements This project has received funding from the European Union´s Horizon 2020 research and innovation programme under the Marie Sklodowska-Curie grant agreement No 713694 (MULTIPLY). We acknowledge the use of Athena at HPC Midlands+, which was funded by the EPSRC on grant EP/P020232/1 as part of the HPC Midlands+ consortium.

1) J. Lu, F. Shi, J. Xu, L. Meng, L. Zhang, P. Cheng, X. Zhou, F. Pang, and X. Zeng, Nanophotonics **10**, 983 (2021).

2) I.B. Javorsky, R.E. Silva, and A.A.P. Pohl, IEEE Photonics Technol. Lett. **31**, 1135 (2019).

3) A.A.P. Pohl, R.A. Oliveira, R.E. Silva, C.A.F. Marques, P. de T. Neves, K. Cook, J. Canning, and R.N. Nogueira, Photonic Sensors **3**, 1 (2013).

4) R.E. Silva, M. Becker, M. Rothhardt, H. Bartelt, and A.A.P. Pohl, J. Light. Technol. **36**, 4146 (2018).

5) R.E. Silva, T. Tiess, M. Becker, T. Eschrich, M. Rothhardt, M. Jäger, A.A.P. Pohl, and H. Bartelt, Laser Phys. Lett. **12**, 045101 (2015).

6) I.L. Villegas, C. Cuadrado-Laborde, J. Abreu-Afonso, A. Díez, J.L. Cruz, M.A. Martínez-Gámez, and M.V. Andrés, Laser Phys. Lett. **8**, 227 (2011).

7) W.F. Liu, P.S.J. Russell, and L. Dong, J. Light. Technol. **16**, 2006 (1998).

8) C. Cuadrado-Laborde, A. Diez, M. Delgado-Pinar, J.L. Cruz, and M. V. Andrés, Opt. Lett. **34**, 1111 (2009).

9) H.E. Engan, B.Y. Kim, J.N. Blake, and H.J. Shaw, J. Light. Technol. **6**, 428 (1988).

10) J. Achenbach, *Wave Propagation in Elastic Solids.*, 1st ed. (Elsevier Science, 1984).

11) R.N. Thurston, J. Acoust. Soc. Am. **64**, 1 (1978).

12) R.E. Silva, M.A.R. Franco, P.T. Neves, H. Bartelt, A.A.P. Pohl, P. Neves Jr., H. Bartelt, and A.A.P. Pohl, Opt. Express **21**, 6997 (2013).

13) R.E. Silva, A. Hartung, M. Rothhardt, A.A.P. Pohl, and H. Bartelt, Opt. Commun. **344**, 43 (2015).

14) V. Pagneux, in *Dyn. Localization Phenom. Elasticity, Acoust. Electromagn. CISM Int. Cent. Mech. Sci.* (Springer, 2013), pp. 181–223.

15) J. Liu, Y. Xiong, E. Lu, D. Yang, and Y. Yuan, Appl. Phys. Express **12**, 116503 (2019).

16) X. Xue, P. Li, and F. Jin, Appl. Phys. Express **14**, 044002 (2021).

17) R.E. Silva, M. Becker, M. Rothhardt, H. Bartelt, and A.A.P. Pohl, IEEE Photonics J. **9**, 1 (2017).

18) B.W. Ti, W.D. O'Brien, and J.G. Harris, J. Acoust. Soc. Am. **102**, 1528 (1997).

19) B. Masserey, C. Raemy, and P. Fromme, in *Ultrasonics* (Elsevier, 2014), pp. 1720–1728.

20) L. Pochhammer, J. Fur Die Reine Und Angew. Math., 324 (1876).

21) C. Chree, Q. J. Pure Appl. Math. **21**, 287 (1886).

22) M.L. Peterson, Exp. Mech. **39**, 36 (1999).

23) A.D. Puckett and M.L. Peterson, Acoust. Res. Lett. Online **6**, 268 (2005).

24) A.D. Puckett and M.L. Peterson, Ultrasonics **43**, 197 (2005).

25) A. Puckett, An Experimental and Theoretical Investigation of Axially Symmetric Wave Propagation in Thick Cylindrical Waveguides , 2004.

26) M. Callan, C.M. Linton, and D. V. Evans, J. Fluid Mech. **229**, 51 (1991).

27) O. Frazao, J.M. Baptista, J.L. Santos, J. Kobelke, and K. Schuster, J. Eur. Opt. Soc. Rapid Publ. **4**, (2009).

28) A. Minardo, A. Cusano, R. Bernini, L. Zeni, and M. Giordano, IEEE Trans. Ultrason. Ferroelectr. Freq. Control **52**, 304 (2005).

29) D.C. Betz, G. Thursby, B. Culshaw, and W.J. Staszewski, Smart Mater. Struct. **12**, 122 (2003).

30) N.E. Fisher, D.J. Webb, C.N. Pannell, D.A. Jackson, L.R. Gavrilov, J.W. Hand, L. Zhang, and I. Bennion, Appl. Opt. **37**, 8120 (1998).

31) Y.J. Rao, D.J. Webb, D.A. Jackson, L. Zhang, and I. Bennion, J. Light. Technol. **15**, 779 (1997).